Article

Cell Reports

Convergent Projections from Perirhinal and Postrhinal Cortices Suggest a Multisensory Nature of Lateral, but Not Medial, Entorhinal Cortex

Graphical Abstract

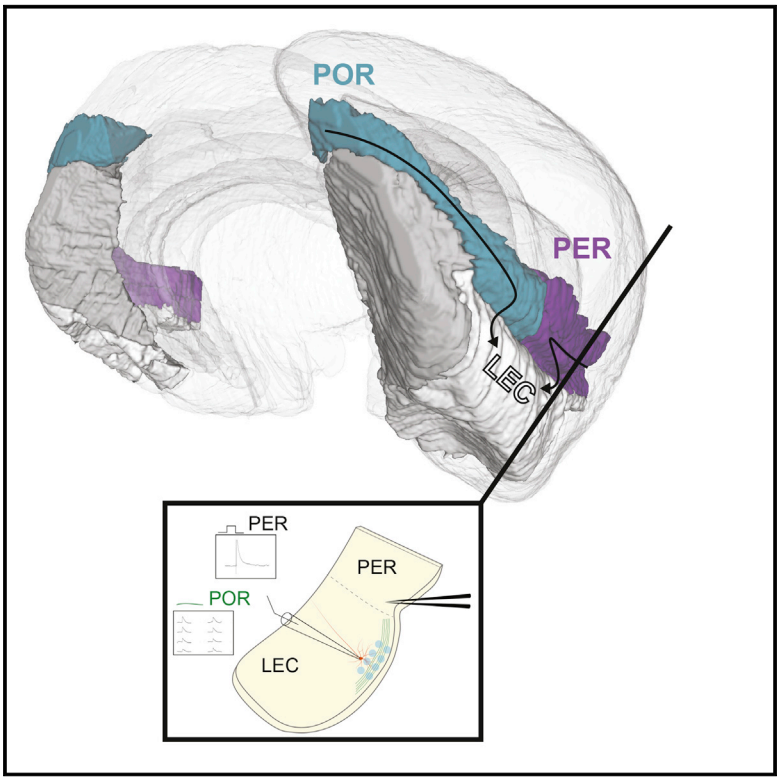

Highlights

- Postrhinal cortex preferably targets lateral instead of medial entorhinal cortex
- Postrhinal and perirhinal projections converge on lateral entorhinal layer 2 cells
- Lateral entorhinal cortex is the main parahippocampal multimodal integrative area
- A comparable input organization scheme likely exists in the primate

Authors

Thanh P. Doan, Maria J. Lagartos-Donate, Eirik S. Nilssen, Shinya Ohara, Menno P. Witter

Correspondence

menno.witter@ntnu.no

In Brief

Doan et al. demonstrate with the use of tract tracing and *in vitro* electrophysiological recordings that the rat lateral entorhinal cortex receives convergent perirhinal and postrhinal inputs. They further argue that a comparable input organization scheme also exists in the primate, challenging the prevailing concept of parallel parahippocampal pathways to the hippocampus.

Doan et al., 2019, Cell Reports *29*, 617–627
October 15, 2019
https://doi.org/10.1016/j.celrep.2019.09.005

CellPress

Cell Reports
Article

Convergent Projections from Perirhinal and Postrhinal Cortices Suggest a Multisensory Nature of Lateral, but Not Medial, Entorhinal Cortex

Thanh P. Doan,[1] Maria J. Lagartos-Donate,[1] Eirik S. Nilssen,[1] Shinya Ohara,[2] and Menno P. Witter[1,3,*]
[1]Kavli Institute for Systems Neuroscience, Centre for Computational Neuroscience, Egil and Pauline Braathen and Fred Kavli Centre for Cortical Microcircuits, NTNU Norwegian University of Science and Technology, Trondheim, Norway
[2]Laboratory of Systems Neuroscience, Tohoku University Graduate School of Life Science, Sendai, Japan
[3]Lead Contact
*Correspondence: menno.witter@ntnu.no
https://doi.org/10.1016/j.celrep.2019.09.005

SUMMARY

The current model of the organization of the medial temporal lobe (MTL) episodic memory system assumes that two functionally different "where" and "what" pathways enter MTL as parallel parahippocampal cortex (PHC)-medial entorhinal cortex (MEC) and perirhinal cortex (PER)-lateral entorhinal cortex (LEC) streams, respectively. With the use of tract tracing and *in vitro* electrophysiological recordings, we show that, in the rat LEC, all main principal neuron types in layer II receive convergent inputs from PER and postrhinal cortex (POR), homologous to PHC in primates. Projections to MEC from POR are much less prominent than previously assumed. These findings thus challenge the prevailing concept that LEC and MEC are defined by different inputs from the PER and PHC/POR, respectively. Our findings point to LEC as the main parahippocampal multimodal integrative structure whose unique set of external sensory-derived inputs allows its network to represent a continuously fluctuating extrinsic environment.

INTRODUCTION

The entorhinal cortex (EC) is the main hub connecting the cortex with the hippocampal formation (HF). Together, EC and HF form the core of the medial temporal lobe episodic memory system (Eichenbaum, 2017; Moser et al., 2017). The prevailing notion is that EC is composed of a medial (MEC) and a lateral (LEC) subdivision. Though both LEC and MEC project to the entire longitudinal extent of HF, there is a clear topology such that their more dorsal and lateral parts project predominantly to dorsal parts of HF (Witter et al., 1989). The current model of the organization of the parahippocampal region (PHR) assumes that two functionally different "where" and "what" pathways enter the medial temporal lobe as parallel streams, mediated by parahippocampal cortex (PHC)-MEC and perirhinal cortex (PER)-LEC connections, respectively. According to this model, the two streams eventually converge within HF, which combines the two information streams into a complete memory representation (Eichenbaum et al., 2007; Ranganath and Ritchey, 2012; Yonelinas and Ritchey, 2015). This model is based on several seminal neuroanatomical studies that have been taken to indicate that PHC (in primates, homologous to the postrhinal cortex [POR] in rodents) carrying visuospatial information and PER carrying object information are among the principal and categorical inputs to MEC and LEC, respectively (Suzuki and Amaral, 1994; Naber et al., 1997; Burwell and Amaral, 1998b; Schultz et al., 2012; Maass et al., 2015; Navarro Schröder et al., 2015).

The more dorsal parts of MEC contain a high percentage of spatially modulated neurons, such as grid, head direction, border, aperiodic spatial, and object-vector cells, i.e., parameters necessary for spatial navigation (Hafting et al., 2005; Sargolini et al., 2006; Solstad et al., 2008; Doeller et al., 2010; Killian et al., 2012; Jacobs et al., 2013; Miao et al., 2017; Høydal et al., 2019). In contrast, dorsolateral parts of LEC contain neurons and networks representing information about objects and their complexity, object traces over time, and sequences of an event, i.e., parameters relevant in the realm of representing the specific content and temporal order of an ongoing experience (Deshmukh and Knierim, 2011; Tsao et al., 2013, 2018; Van Cauter et al., 2013; Wilson et al., 2013a, 2013b; Reagh and Yassa, 2014; Rodo et al., 2017; Wang et al., 2018; Montchal et al., 2019). Notwithstanding these striking functional differences, the main hippocampal-projecting cell types in both entorhinal subdivisions are embedded into an overall comparable local circuit architecture (Couey et al., 2013; Pastoll et al., 2013; Fuchs et al., 2016; Leitner et al., 2016; Nilssen et al., 2018; Ohara et al., 2018). Therefore, it is likely that specific input sets to each EC subdivision contribute fundamentally to their functional differences (Nilssen et al., 2019).

In the present paper, we test whether the current model of MTL organization described above is correct. In contrast to that model, we demonstrate anatomically that, in the rat, the entorhinal projections originating in POR preferentially target LEC instead of MEC. *In vitro* electrophysiology corroborates the observation of strong POR inputs to LEC and further shows that these inputs converge with PER inputs onto all main principal cell types in layer II. Using available anatomical data in the non-human primate, we argue that a comparable input

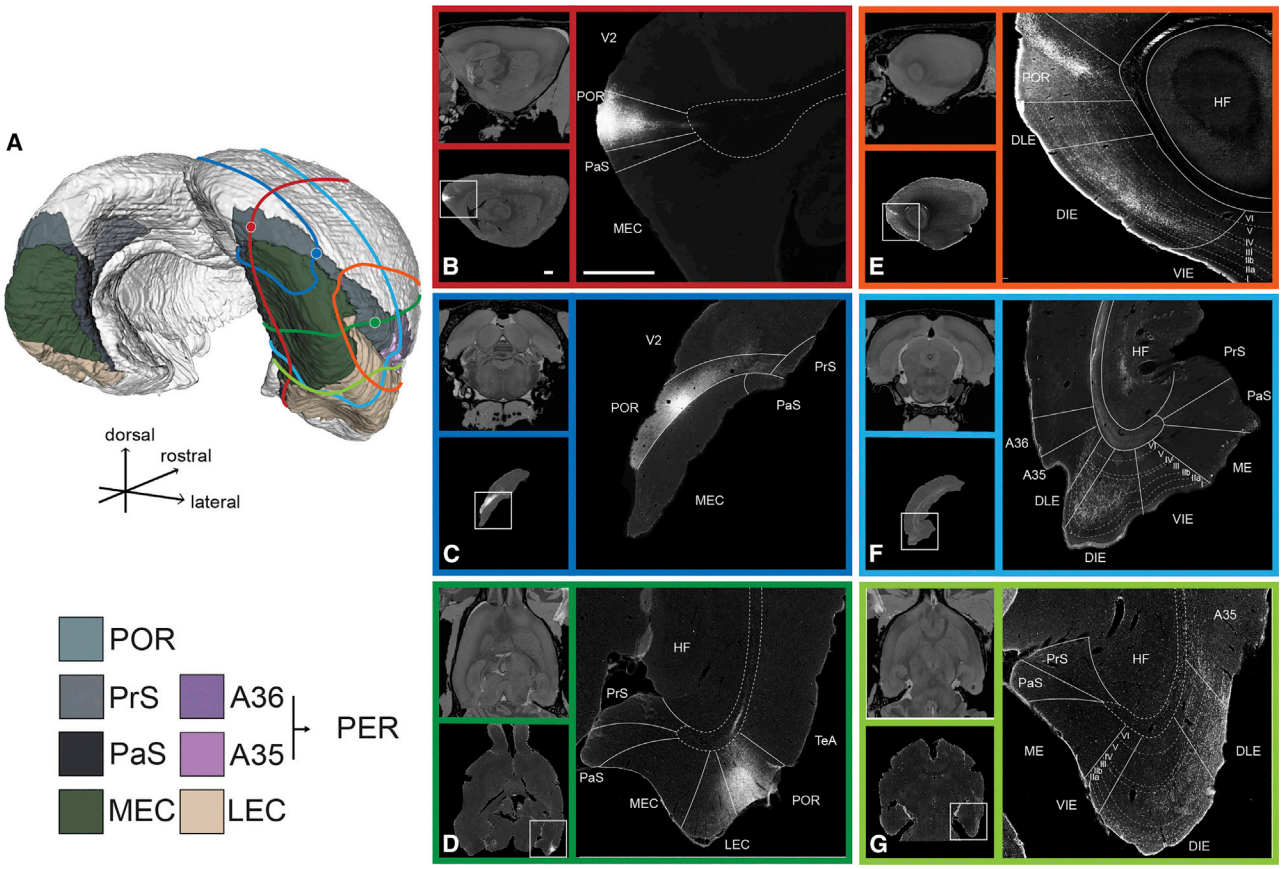

Figure 1. Distribution of POR Axon Terminals into LEC

(A) 3D Waxholm Space model (WHS) (based on *ex vivo* ultra-high-resolution MRI with PHR cytoarchitectural delineations corroborated in all main anatomical plans; Papp et al., 2014; Boccara et al., 2015) with 3 representative POR injections at different positions along its longitudinal extent.

(B) Sagittal section showing an injection in caudomedial POR.

(C) Coronal section showing an injection in mid-caudorostral POR.

(D) Horizontal section with an injection in rostrolateral POR.

(E) Sagittal section demonstrating anterogradely labeled projections of caudomedial POR in LEC.

(F) Coronal section demonstrating mid-caudorostral POR projections into LEC.

(G) Horizontal section demonstrating rostrolateral POR projections into LEC.

(B–G) MRI plane section from WHS (upper left panel), corresponding to the complete histological section (lower left panel) and high-power images taken from the area indicated by the white square in complete histological section (right panel). Scale bar in low- and high-power histological sections in (B) equals 1,000 μm and applies to all histological sections (B)–(G). See Figure S1 for definitions of subdivisions of EC and Videos S1 and S2, Tables S1 and S2, and Figure S2 for details on anterograde and retrograde cases.

organization scheme likely exists in the primate as well. Our findings thus challenge the concept that the two functionally different parallel HF input pathways mediated by MEC and LEC are defined by their respective inputs from the two adjacent parahippocampal POR/PHC and PER domains. Our data clearly indicate that LEC receives strong inputs from both domains and that projections of POR to MEC are less prominent. These data lead to an altered functional connectional model of PHR in which LEC represents a main integrative input structure for the hippocampus.

RESULTS

In the rodent, POR is one of the three main components of the six-layered rhinal cortex together with PER and EC (Figure 1). Out of these three, POR is the caudomedial-most area and it is composed of a ventral (PORv) and a dorsal (PORd) subdivision (Burwell, 2001). Likewise, the rostrolateral PER comprises a ventral (A35) and a dorsal (A36) subdivision (Burwell et al., 1995). Both POR and PER run almost parallel with the rhinal fissure, occupying the fundus and/or its dorsal and ventral banks. These two areas, in association with the rhinal fissure, mark the lateral and dorsal border of EC. In the current paper, we divide EC into MEC composed of caudal (CE) and medial (ME) subdivisions and LEC composed of dorsal lateral (DLE), dorsal intermediate (DIE), and ventral intermediate (VIE) subdivisions (Insausti et al., 1997; Figure S1).

POR is located caudal to PER and mostly dorsal to the rhinal fissure, where it rises steeply and wraps obliquely around the caudal pole of EC. POR cytoarchitecture features a homogeneous neuronal distribution across layers II–IV and a resulting

lack of a prominent laminar structure. Nonetheless, PORd cells in layer III appear more organized with a clear radial appearance that is absent in PORv (Burwell 2001). Similar to A35, PORv is completely devoid of parvalbumin (PV) positivity, and PORd stains stronger for PV similarly to A36. The distribution of calbindin (Cb) neuropil in PORv is also similar to that in areas 35 and 36, respectively. PORv is bordered ventrally by EC for the most part, which is, however, replaced caudomedially by a highly variable dorsolateral extension of the parasubiculum (PaS), which can easily be mistaken for MEC (Burgalossi et al., 2011; Boccara et al., 2015; Ramsden et al., 2015; Tang et al., 2016). A striking feature of PaS is its lack of a clear differentiation between superficial layers II and III, seen in dorsal CE, whereas its neuron diameters are substantially larger than the one seen in POR. In addition, PaS markedly lacks reactivity for Cb in its superficial layers, which contrasts with the moderate to strong reactivity for that protein of the superficial layers of EC and POR. PV staining also makes these borders stand out because MEC and PaS superficial layers stain strongly for PV, contrary to PORv. The anterior border of POR is with PER, slightly rostral to the ventrally adjacent border between DLE and CE. The rostral border of PER is with the insular cortex, and this border in coronal sections coincides with the emergence of the claustrum deep to the insular cortex (Burwell, 2001). The border between LEC and A35 is indicated by the loss of the typical lamina dissecans in LEC. The superficial layers of A35 are homogeneously packed with small neurons, whereas DLE demonstrates a clear lamination in its superficial layers, with layer II cells being larger and more darkly stained than layer III cells. Besides, superficial layers of DLE stain heavily for PV, although such staining is essentially absent in A35. Vice versa, in material stained for Cb, a marked increase of staining in area 35 is noticeable. At last, each EC subdivision is differentiated based on subtle cytoarchitectonic differences and mainly serve detailed anatomical comparisons, but a general pattern is that deep layers (V and VI) are clearly distinguishable from superficial layers (II and III), as the thin acellular layer IV, i.e., lamina dissecans, separates them, and this is particularly well developed in MEC. In the present paper, a border of interest is between the two MEC subdivisions, i.e., areas CE and ME. The most striking change that defines this border is an overall less conspicuous lamination in ME than in CE. The superficial layers of ME are less homogeneous than their CE counterparts: ME layer II breaks up into two or three clusters of cells, which makes it less sharply delineated from both layers I and III and ME layer III tends to split into sublayers. Differences exist also in the superficial portion of their deep layers (layer Va, in opposition to layer Vb), as CE layer Va is sparsely populated by large pyramidal cells and ME is characterized by a more regularly structured layer Va with a higher number of large pyramidals positioned at regular intervals. Finally, the superficial layers of ventral CE exhibit moderate homogeneous reactivity for parvalbumin, unlike ME, where the staining is less strong to absent (Figure S1).

POR Projections to LEC Are Extensive and Comparable to Their PER Counterparts

Analysis of all POR anterograde injections (n = 64) in our multiplane library (Video S1; Table S1) revealed that the entire POR projects strongly to the full rostrocaudal extent of LEC. Anterogradely labeled terminal axons were densest in LEC superficial layers and restricted to its more dorsal and lateral parts, including DLE and DIE, whereas the ventral-intermediate part of LEC (VIE) was virtually devoid of POR fibers (Figure 1). Branching axons with synapse-like varicosities were seen in deep layer (L)I and LIIa, showing an increased density in LIIb and throughout LIII. Labeling in deeper layers was weak or absent, except in DLE, where a moderate density of axonal terminal labeling could be observed. The POR projections to LEC showed a topographical organization such that caudal and medial parts of POR projected densest to DIE, and projections that originated in increasingly more lateral and rostral parts of POR progressively shifted toward the rhinal fissure into DLE (Figures 1E–1G, right panels). All anterograde injections involving superficial layers of PORv resulted in very dense labeling in superficial LEC, and the ones confined to PORd resulted in comparably distributed but weaker labeling. In contrast, injections confined to deep layers of POR labeled only minor projections to deep layers of DLE.

To further characterize POR projecting neurons, we injected the retrograde tracers cholera toxin subunit B (CTB) (n = 3) or Fluorogold (FG) (n = 2) in the dorsolateral LEC of adult rats (Figures S2A and S2B; Video S2; Table S2). In POR, the majority of retrogradely labeled cells were located in LII/III (78.4% or n = 3,044/3,885 cells; σ = 9.4; n = 5; Figure S2B). These injections were made through vertically oriented glass pipettes, which thus enter LEC through PER. This may have caused some tracer leakage into PER, explaining the more or less equal distribution of retrogradely labeled neurons in PORv and PORd, which did not seem in line with our anterograde tracing data. To control for possible leakage along the needle track, we assessed additional retrograde FG injections (n = 4), deposited directly into superficial layers of dorsolateral LEC through laterally drilled burr holes (Figures S2A–S2C; Video S2; Table S2). In all latter cases, retrogradely labeled neurons were present almost exclusively in a clear band spreading across PORv LII/III, confirming our anterograde observations that superficial layers of PORv originate most of the projection to superficial layers of LEC (Figure S2C). Because LII/III of POR/PHC contain a significant number of Calbindin (Cb)-positive cells in mammals (Suzuki and Porteros, 2002; Uva et al., 2004; Boccara et al., 2015), we assessed whether LEC-projecting POR neurons included Cb-positive cells. Immunostaining against Cb showed that over a quarter of superficial POR cells projecting to LEC expressed Cb (27.2% or n = 828/3,044 cells; σ = 1.1; n = 5; Figures S2D and S2E).

Next, we confirmed in our dataset of anterograde tracer injections in PER (n = 23) that PER projected mainly to LEC II and III (Burwell and Amaral, 1998a). In line with previous reports (Burwell and Amaral, 1998b), our data show that these projections mainly target DIE and DLE, with a clear preference for DLE in case of rostral PER injections (Figures S2F–S2H). Additionally, A35 (ventral PER) sends stronger projections to LEC than A36 (dorsal PER; Burwell and Amaral, 1998b). We thus conclude that dorsolateral parts of LEC receive inputs from both POR and PER and that both these projections show very similar topological features, indicative of a potential for convergent innervation of neurons in dorsolateral LEC.

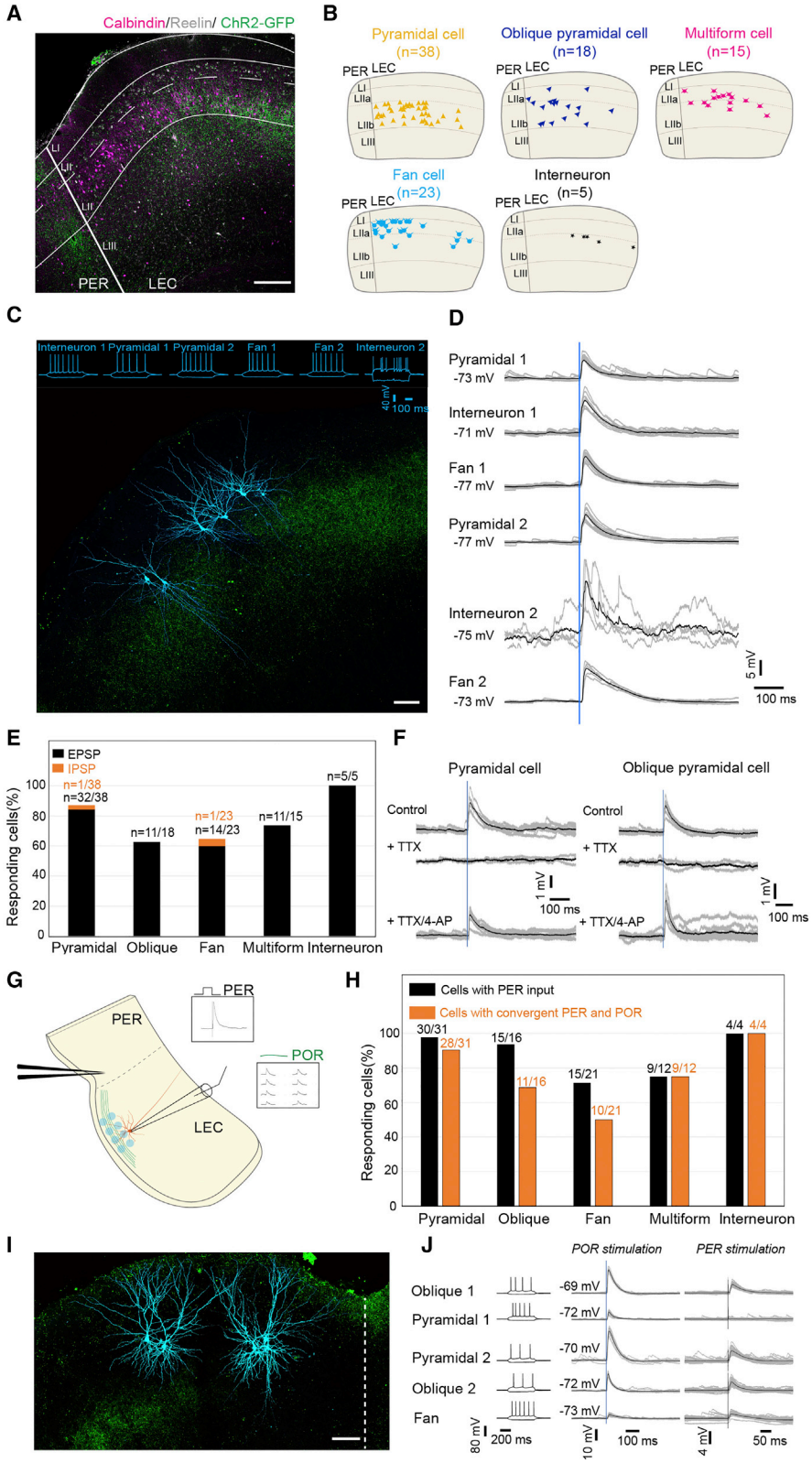

(legend on next page)

Single LEC II Cells Receive Convergent PER and POR Monosynaptic Inputs

We next assessed whether the anatomically established POR to LEC projections form functional inputs to LEC and aimed to determine the postsynaptic targets in LEC. We carried out *in vitro* current clamp recordings of single LEC LII neurons in slices prepared from animals, in which the POR axonal projections were expressing the light-sensitive cation channel channelrhodopsin2 (ChR2). Injection of an adeno-associated virus (AAV) (AAV1.hSyn.ChR2(H134R)-eYFP.WPRE.hGH) into POR in female and male rats (n = 13) resulted in a clearly identifiable plexus of yellow fluorescent protein (YFP)-positive axons in layers II and III of LEC, allowing us to photostimulate the labeled axons and presynaptic terminals. It is well established that layer II in LEC comprises two main types of principal cells, which are characterized by the selective expression of the molecular markers reelin and calbindin (Figure 2A). Reelin-positive neurons are the ones that project to the dentate gyrus, and all fan cells belong to this chemically defined cell group. In contrast, calbindin-positive neurons do not contribute to this projection and send their axons to a number of extrahippocampal targets as well as contribute to inter- and intra-entorhinal excitatory projections (Leitner et al., 2016; S. Ohara et al., 2016, Soc. Neurosci., abstract; Witter et al., 2017). We therefore used post hoc immunohistochemistry to differentiate between reelin- and calbindin-positive neurons that are mainly confined, respectively, to superficial or deep layer II (layer IIa and IIb, respectively; Figure 2A). We recorded from principal cells (n = 94) located in layer IIa (n = 28) and IIb (n = 66). We classified principal cells based on post hoc characterization of somato-dendritic morphology, in accordance with established morphological descriptions and reports that electrophysiological properties are not or only weakly correlated with neuronal morphology (Canto and Witter, 2012; Leitner et al., 2016; Desikan et al., 2018; Nilssen et al., 2018). We found that most recorded cells displaying a pyramidal-like (pyramidal and oblique pyramidal) morphology were located in layer IIb (n = 53/56), whereas most recorded cells displaying a fan cell morphology were located in layer IIa (n = 17/23; Figure 2B; Tahvildari and Alonso, 2005; Canto and Witter, 2012; Leitner et al., 2016; Nilssen et al., 2018). Optogenetic stimulation of ChR2-labeled POR fibers elicited responses across all main classes of layer II principal cells in LEC (74% or n = 70/94 cells), in addition to a small number of recorded putative inhibitory interneurons (n = 5; Figures 2C–2E). Recorded potentials were in most cases excitatory (97% or n = 68/70 cells), though inhibitory postsynaptic potentials were detected in one fan and one pyramidal cell. In a subset of recorded cells (n = 4 cells from 3 rats), we demonstrated through bath application of tetrodotoxin (TTX) (1 μM) and 4-aminopyridine (4-AP) (100 μM) that these excitatory postsynaptic potentials reflected monosynaptic inputs from POR axons (Figure 2F; Petreanu et al., 2009).

To test whether cells postsynaptic to POR inputs were also recipients of PER synaptic inputs, we also applied electrical stimulation of PER by way of a bipolar extracellular electrode in the superficial layers of PER (de Villers-Sidani et al., 2004; T.P. Doan et al., 2016, Soc. Neurosci., conference), immediately adjacent to the LEC border (Figure 2G). We have previously shown that activation of neurons in PER by way of photostimulation of caged glutamate elicits excitatory postsynaptic potentials in simultaneously recorded LEC layer II principal cells. Neurons providing synaptic inputs to LEC were found within a ventral portion of PER adjacent to LEC, and electrical stimulation in that ventral area consistently resulted in postsynaptic potentials in recorded LEC layer II cells (T.P. Doan et al., 2016, Soc. Neurosci., conference). Hence, we reasoned in the present study that extracellular electrical stimulation of this same ventral portion of PER is suitable to activate the pathway connecting PER to LEC. Similar to POR inputs, excitatory postsynaptic potentials evoked by activation of PER were detected in all

Figure 2. PER and POR Inputs Converge on Single LEC II Cells

(A) Axonal projections (green) from postrhinal cortex (POR) mainly target LIIb and LIII of the lateral entorhinal cortex (LEC). Reelin (white) and calbindin immunoreactivity (magenta) delineate superficial LIIa, deep LIIb, and LIII. Scale bar: 200 μm.

(B) Distribution of recorded cells according to morphological type in LII of LEC.

(C) Six current clamp recorded LEC LII cells (two interneurons, two pyramidal cells, and two fan cells; cyan) in the same slice together with POR afferent fibers (green). For each recorded cell, electrophysiological responses to weak depolarizing and hyperpolarizing current step injections are shown (top of panel). Scale bar: 100 μm.

(D) Excitatory postsynaptic potentials recorded from the cells in (C) during a single laser stimulation pulse of ChR2-expressing axons originating in POR. The average resting potential at which connectivity was tested is indicated for each cell.

(E) Distribution of recorded cells in LEC layer II receiving synaptic inputs in response to optogenetic activation of POR axons. Cells are grouped according to morphological type.

(F) Monosynaptic POR inputs to LEC LII neurons. Shown are traces from a pyramidal and an oblique pyramidal cell (top row) demonstrating that synaptic responses are action potential dependent (+TTX, middle row) and can be partially recovered by the addition of 4-AP (+TTX/4-AP, bottom row).

(G) Schematic of the experiment to demonstrate convergence of synaptic inputs from PER and POR onto LEC LII cells. Current clamp recordings of cells in LII of LEC during optogenetic stimulation (blue circles) of ChR2-labeled axonal fibers (green) following AAV injection in POR. Electrical stimulation with a bipolar electrode in PER is used to demonstrate PER input onto LEC LII cells. Insets: example synaptic responses following a single stimulation pulse of PER (left) and synaptic responses following grid patterned laser-scanning photostimulation of POR fibers (right) are shown.

(H) Distribution of recorded LEC LII cells receiving PER inputs (black) and convergent PER and POR inputs (orange).

(I) Five current clamp recorded LEC LII cells (two oblique pyramidal cells, two pyramidal cells, and one fan cell; cyan) together with afferent Chr2-labeled POR fibers (green). Dotted line indicates the border with PER. Scale bar: 100 μm.

(J) Electrophysiological responses to weak depolarizing and hyperpolarizing current step injections (left) for each of the recorded cells in (I). Middle and right panels show recorded synaptic responses for the five cells to POR and PER stimulation, respectively. Time of stimulation is indicated by the blue and black vertical lines, respectively. The average resting potential at which connectivity was tested is indicated for each cell.

See also Figure S2I.

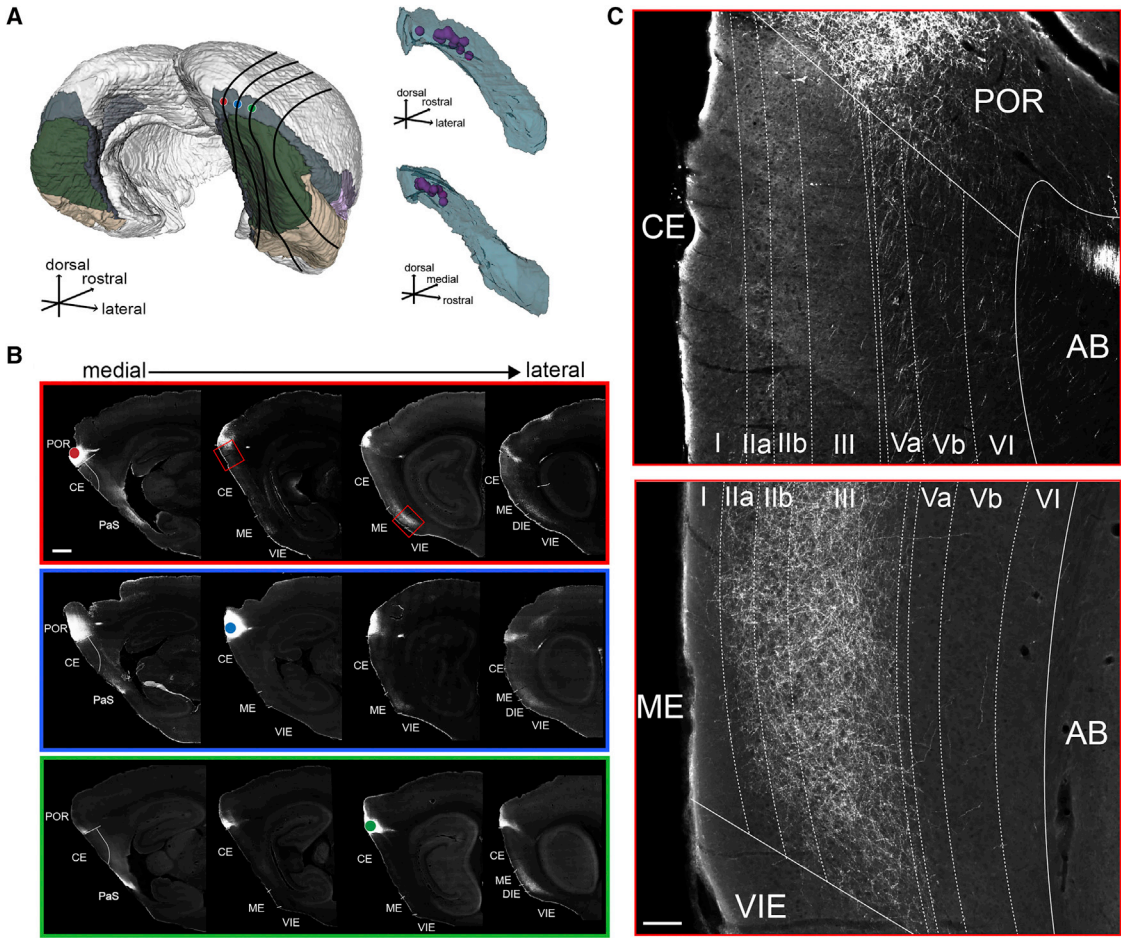

Figure 3. Distribution of POR Axon Terminals into MEC

(A) 3D WHS model with 3 representative injections distributed in caudomedial POR (left panel) and isolated POR 3D representation with center of mass of all pure anterograde injections (purple) that resulted in dense projections in MEC (caudal and lateral views in upper and lower right panels, respectively).

(B) POR projections from the 3 injections in (A), left panel, showing distributions in PHR at 4 sagittal levels corresponding to the black lines in (A). Colored dots indicate the center of mass of each injection site. Labeled axonal terminal plexus in MEC appears always laterally from the injection sites. Red square boxes in upper panels are insets displayed at higher magnification in (C), representing typical axonal labeling in dorsal MEC (area CE) and ventromedial MEC (area ME). Scale bar: 1,000 μm.

(C) Magnification of areas marked with an asterisk in red square boxes in upper (B). Panels demonstrating representative POR axonal distribution in dorsal MEC (area CE; upper panel) and ventromedial MEC (area ME; lower panel) are shown. Scale bar: 100 μm.

See Figure S1 for delineations of subdivisions of EC and Figure S3 for additional anterograde and retrograde material.

principal cells groups as well as a small group of putative inhibitory interneurons (Figure 2H). Most of the synaptic potentials recorded in principal cells and putative interneurons following stimulation of PER were presumed monosynaptic (74%; n = 54/73 cells), evident by minimal jitter (<700 μs) in the observed onset latencies. Recorded postsynaptic potentials following extracellular PER activation were abolished by bath application of TTX (1 μM; n = 8 from 3 rats), indicating that these were not evoked by direct volume conduction but instead required action-potential-induced release of neurotransmitter (Figure S2I). The majority of principal cells (73%; n = 58/80) that were tested for both inputs responded to POR optogenetic stimulation as well as extracellular electrical stimulation of PER (Figures 2H–2J). Taken together, our data show that projections from POR provide input to all main principal cell types in layer II of LEC and that these cells very likely also receive additional input from PER.

POR Projections to the Canonical Spatially Modulated MEC Are Relatively Sparse

Injections in both PORd and PORv resulted in terminal-like labeling as well as labeled passing fibers ventrally and laterally in deep layers of the caudodorsal part of MEC (area CE) with a notable preference for LVa. The labeled passing fibers continued ventrally reaching area ME, where they collateralized abundantly in superficial layers (Figures 3A–3C). This specific pattern, including the dense terminal labeling in superficial layers of ventral MEC, was only seen following injections in a restricted caudomedial portion of POR (Figure 3A, right panel; for lack of POR projections in area ME

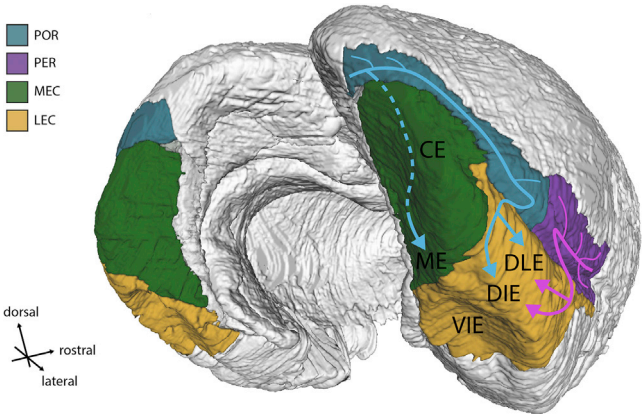

Figure 4. Schematic Summary of POR and PER Connectivity to EC
Summarized projections of POR and PER to superficial layers of EC showing a strong preference for lateral parts of LEC (DLE and DIE). For more details, see Figure S4.

following injections in lateral and rostral POR, see Figures 1A, 1F, and 1G).

Next, we searched our entire dataset for injections that resulted in dense projections to superficial layers of dorsal MEC (area CE), as reported in previous studies (Naber et al., 1997; Burwell and Amaral, 1998b; Koganezawa et al., 2015). This assessment showed that all injections resulting in the aforementioned pattern involved labeling of the ventrally positioned PaS or dorsal MEC (n = 12), meticulously delineated with a complementary triple immunostaining procedure of NeuN, Cb, and PV (Figures S3A and S3B; Boccara et al., 2015). None of the injections that were confined to PORv showed terminal labeling in superficial layers of the dorsal MEC subdivision CE (Figures 3C, upper panel, and S3D). The conclusion that superficial layers of dorsal MEC indeed receive only minimal POR input was corroborated by a series of retrograde tracer injections in superficial layers of CE (n = 4; Figure S3A). In all cases, we observed many retrogradely labeled cells in the thin dorsolateral extension of PaS intercalated between PORv and caudodorsal CE, whereas the immediate neighboring POR contained hardly any labeled somata (Figure S3C). The dorsolateral extension of PaS, notorious for its highly variable neuroanatomical boundaries (Burwell et al., 1995; Burgalossi et al., 2011; Boccara et al., 2015; Ramsden et al., 2015; Tang et al., 2016), projects indeed ventrally to layer II of dorsal MEC (Caballero-Bleda and Witter, 1993).

In conclusion, our anterograde and retrograde material indicate that superficial layers of the dorsal MEC area CE are largely devoid of POR inputs, which is in line with previously published data using retrograded rabies tracing of specific inputs to layer II of dorsal MEC (Rowland et al., 2013). In contrast, superficial layers of the more ventrally positioned area ME receive strong projections from the caudomedial portions of POR (Figures 3A, right panels; 3C, lower panel; 4; and S4). It is of particular interest that even the most ventral MEC recordings of spatially modulated cells were still confined within area CE (Brun et al., 2008; Stensola et al., 2012). Thus, area ME remains to this day a functionally unexplored area whose role seems in fact unrelated to spatial navigation memory, contrasting with the canonical spatially modulated area CE (Steffenach et al., 2005).

DISCUSSION

The present findings directly challenge the core anatomical principle of the current model on the organization of the medial temporal lobe episodic memory system and point to LEC as a unique site of convergence within PHR (Figures 4 and S4). Although our observations may seem in conflict with prior studies, a careful reanalysis of the projection patterns as described in the seminal work of Burwell and Amaral (1998b) actually supports our findings. Their data factually show that POR projections preferentially terminate dorsolaterally in LEC (64.5%; $\sigma = 13.1$; n = 3), along its rostrocaudal extent. In contrast, the projections to MEC are less strong (35.5%; $\sigma = 13.1$; n = 3) and largely restricted to ventral MEC, likely corresponding to area ME (Figures S5A–S5C). Furthermore, re-evaluation of available non-human primate tract tracing data on entorhinal projections from the PHC, the likely homolog of the rodent POR, reveals similarities with our current description in the rat. First, PHC projects obliquely from caudomedial to rostrolateral EC (Insausti et al., 1987; Suzuki and Amaral, 1994; Insausti and Amaral, 2008), similar to the oblique distribution of projections from POR that extend from medioventral (area ME) to rostrolateral EC (areas DIE and DLE; present study). Second, both caudal and rostral PHC emit projections spanning the rostrocaudal extent of LEC (Insausti et al., 1987; Suzuki and Amaral, 1994; Insausti and Amaral, 2008). Third, a restricted portion of caudal PHC seems to originate the main projections to caudomedial EC (Suzuki and Amaral, 1994; Insausti and Amaral, 2008), akin to the restricted portion of caudomedial POR projecting to medioventral area ME (current data). Fourth, PHC projections to LEC show a topographical organization similar to the rodent, such that caudal PHC projects densest to mediolateral levels of LEC and projections that originate in increasingly more rostral parts of PHC appear to progressively shift laterally toward the collateral sulcus (lateral rostral and lateral caudal entorhinal cortex subfields; areas ELr and ELc, respectively) EC (Insausti and Amaral, 2008). Therefore, PHC projects to an LEC area positioned close to the collateral sulcus, i.e., similar to the rodent dorsolateral LEC, which is close to the rhinal fissure (Kobro-Flatmoen and Witter, 2019). Finally, in this lateral area in the monkey, similar to what we showed in the present paper for POR and PER inputs, PHC and PER inputs seemingly converge in EC (Insausti et al., 1987; Suzuki and Amaral, 1994; Insausti and Amaral, 2008). Thus, we propose that LEC integrates POR/PHC and PER inputs as well as almost all other cortical inputs that distribute to EC (Insausti et al., 1987; Vaudano et al., 1991; Burwell and Amaral, 1998a; Jones and Witter, 2007; Kerr et al., 2007; Kondo and Witter, 2014; Mathiasen et al., 2015). Exceptions are inputs originating from the presubiculum (PrS) and the retrosplenial cortex (RSC), which are unique for MEC in all species studied so far (Amaral et al., 1984; Köhler, 1984; Saunders and Rosene, 1988; van Groen and Wyss, 1990; Wyss and Van Groen, 1992; Caballero-Bleda and Witter, 1993; Honda and Ishizuka, 2004; Jones and Witter, 2007; Kobayashi and Amaral, 2007). Neurons in LEC further receive inputs from MEC and PaS (Köhler, 1986; Caballero-Bleda and Witter, 1993; Dolorfo

and Amaral, 1998; Chrobak and Amaral, 2007). Recently, we have shown that neurons in LEC layer II integrate PER inputs with other main cortical inputs targeting superficial layers of LEC, i.e., inputs from piriform cortex, MEC, and contralateral LEC (T.P. Doan et al., 2016, Soc. Neurosci., conference). Together, the available data point to a unique multimodal nature of LEC, supported by a network analysis of over 16,000 articles of histologically defined axonal connections, revealing that LEC holds the richest set of association connections of any cerebral cortical region in the rat (Bota et al., 2015).

When focusing on cortical inputs to the superficial layers, the described input features of LEC in both rodents and non-human primates are thus strikingly different from those to superficial layers of MEC, which are restricted to PrS, PaS, and contralateral MEC (Cappaert et al., 2015). The PrS contains the highest proportion of sharply tuned head direction (HD) cells, inherited from a selective input from the anterior thalamic complex (Boccara et al., 2010; Cullen and Taube, 2017). In line with predictions from path-integration models (Burak and Fiete, 2006; McNaughton et al., 2006; Bush and Burgess, 2014), MEC grid cells intrinsically contain this HD signal (Bonnevie et al., 2013), which is fundamental, because disruption of the HD input leads to loss of their grid cell phenotype (Winter et al., 2015). The other exclusive MEC input structure, RSC that selectively targets layer V (Czajkowski et al., 2013), has also been portrayed as providing visuospatial information to the PHR-HF system (Julian et al., 2018), because it contains HD cells and is involved in their relationships to available landmarks in the environment, similar to what has been reported for PrS and PaS (Peck and Taube, 2017).

In contrast, the POR network encodes, monitors, and updates representations of the visuospatial context (Furtak et al., 2012), in line with its recently reported retinotopic representation, which is apparently unique to the parahippocampal region (Burgess et al., 2016) and specific potential to discriminate moving objects (Beltramo and Scanziani, 2019). In the present study, we demonstrate that POR projects strongly to superficial layers of dorsolateral LEC and not to MEC (area CE) as previously assumed. Interestingly, the integration of POR input with other externally driven sensory inputs in the LEC network fits with data indicating that neurons in LEC encode object complexity and object-place-context associations as well as egocentric bearing of the external world (Deshmukh and Knierim, 2011; Tsao et al., 2013; Van Cauter et al., 2013; Wilson et al., 2013a, 2013b; Rodo et al., 2017; Wang et al., 2018). At the population level, LEC cells have been found to code for episodic time, reflecting sequences of events within an episode (Tsao et al., 2018; Montchal et al., 2019). We thus propose that the convergence of a unique set of external sensory-derived inputs allows the LEC network to faithfully represent a continuously fluctuating extrinsic environment.

STAR★METHODS

Detailed methods are provided in the online version of this paper and include the following:

- KEY RESOURCES TABLE
- LEAD CONTACT AND MATERIALS AVAILABILITY
- EXPERIMENTAL MODEL AND SUBJECT DETAILS
- METHOD DETAILS
  - Surgeries
  - Histology and immunohistochemistry of neuroanatomical tracing slices
  - POR borders and delineations
  - PER borders and delineations
  - EC borders and delineations
  - PaS borders and delineations
  - Anatomical tracing studies analysis
  - Construction of two-dimensional unfolded flatmap
  - Electrophysiological slice preparation
  - *In vitro* electrophysiology protocol
  - Optogenetic stimulation of POR fibers
  - Extracellular stimulation of PER
  - Histology and immunohistochemistry of electrophysiological slices
  - Confocal microscopy and EC cell classification
- QUANTIFICATION AND STATISTICAL ANALYSIS
  - Quantification of POR axon terminals in MEC and LEC
  - Optogenetic stimulation of POR fibers
  - Extracellular stimulation of PER
- DATA AND CODE AVAILABILITY

SUPPLEMENTAL INFORMATION

Supplemental Information can be found online at https://doi.org/10.1016/j.celrep.2019.09.005.

ACKNOWLEDGMENTS

We thank Grethe Mari Olsen, Bruno Monterotti, Paulo Girão, and Hanne Tegnander Soligard for technical help; in particular, Paulo Girão helped with the cell colocalization counts that led to Figures S2A–S2E. We also thank Jørgen Sugar and Maximiliano Nigro for their comments on the manuscript. We further thank the staff in the animal facility at the Kavli Institute for Systems Neuroscience. This work was supported by Research Council of Norway grant 227769, the Kavli Foundation, United States, the Centre of Excellence scheme of the Research Council of Norway-Centre for Neural Computation grant 223262, and the National Infrastructure scheme of the Research Council of Norway-NORBRAIN grant 197467.

AUTHOR CONTRIBUTIONS

T.P.D. and M.P.W. conceived the study design. T.P.D., M.J.L.D., E.S.N., and S.O. collected the data. All anatomical quantifications were carried out by T.P.D. Data collection and quantification for Figure 2 was carried out by E.S.N. All authors contributed to the discussions that resulted in the current paper, which was written by T.P.D. and M.P.W. All authors approved the final version of the manuscript.

DECLARATION OF INTERESTS

The authors declare no competing interests.

Received: May 20, 2019
Revised: August 6, 2019
Accepted: August 30, 2019
Published: October 15, 2019

REFERENCES

Amaral, D.G., Insausti, R., and Cowan, W.M. (1984). The commissural connections of the monkey hippocampal formation. J. Comp. Neurol. *224*, 307–336.

Beltramo, R., and Scanziani, M. (2019). A collicular visual cortex: neocortical space for an ancient midbrain visual structure. Science *363*, 64–69.

Boccara, C.N., Sargolini, F., Thoresen, V.H., Solstad, T., Witter, M.P., Moser, E.I., and Moser, M.B. (2010). Grid cells in pre- and parasubiculum. Nat. Neurosci. *13*, 987–994.

Boccara, C.N., Kjonigsen, L.J., Hammer, I.M., Bjaalie, J.G., Leergaard, T.B., and Witter, M.P. (2015). A three-plane architectonic atlas of the rat hippocampal region. Hippocampus *25*, 838–857.

Bonnevie, T., Dunn, B., Fyhn, M., Hafting, T., Derdikman, D., Kubie, J.L., Roudi, Y., Moser, E.I., and Moser, M.B. (2013). Grid cells require excitatory drive from the hippocampus. Nat. Neurosci. *16*, 309–317.

Bota, M., Sporns, O., and Swanson, L.W. (2015). Architecture of the cerebral cortical association connectome underlying cognition. Proc. Natl. Acad. Sci. USA *112*, E2093–E2101.

Brun, V.H., Solstad, T., Kjelstrup, K.B., Fyhn, M., Witter, M.P., Moser, E.I., and Moser, M.B. (2008). Progressive increase in grid scale from dorsal to ventral medial entorhinal cortex. Hippocampus *18*, 1200–1212.

Burak, Y., and Fiete, I. (2006). Do we understand the emergent dynamics of grid cell activity? J. Neurosci. *26*, 9352–9354, discussion 9354.

Burgalossi, A., Herfst, L., von Heimendahl, M., Förste, H., Haskic, K., Schmidt, M., and Brecht, M. (2011). Microcircuits of functionally identified neurons in the rat medial entorhinal cortex. Neuron *70*, 773–786.

Burgess, C.R., Ramesh, R.N., Sugden, A.U., Levandowski, K.M., Minnig, M.A., Fenselau, H., Lowell, B.B., and Andermann, M.L. (2016). Hunger-dependent enhancement of food cue responses in mouse postrhinal cortex and lateral amygdala. Neuron *91*, 1154–1169.

Burwell, R.D. (2001). Borders and cytoarchitecture of the perirhinal and postrhinal cortices in the rat. J. Comp. Neurol. *437*, 17–41.

Burwell, R.D., and Amaral, D.G. (1998a). Cortical afferents of the perirhinal, postrhinal, and entorhinal cortices of the rat. J. Comp. Neurol. *398*, 179–205.

Burwell, R.D., and Amaral, D.G. (1998b). Perirhinal and postrhinal cortices of the rat: interconnectivity and connections with the entorhinal cortex. J. Comp. Neurol. *391*, 293–321.

Burwell, R.D., Witter, M.P., and Amaral, D.G. (1995). Perirhinal and postrhinal cortices of the rat: a review of the neuroanatomical literature and comparison with findings from the monkey brain. Hippocampus *5*, 390–408.

Bush, D., and Burgess, N. (2014). A hybrid oscillatory interference/continuous attractor network model of grid cell firing. J. Neurosci. *34*, 5065–5079.

Caballero-Bleda, M., and Witter, M.P. (1993). Regional and laminar organization of projections from the presubiculum and parasubiculum to the entorhinal cortex: an anterograde tracing study in the rat. J. Comp. Neurol. *328*, 115–129.

Canto, C.B., and Witter, M.P. (2012). Cellular properties of principal neurons in the rat entorhinal cortex. I. The lateral entorhinal cortex. Hippocampus *22*, 1256–1276.

Cappaert, N.L.M., Van Strien, N.M., and Witter, M.P. (2015). Hippocampal formation. In The Rat Nervous System, Fourth Edition, G. Paxinos, ed. (Academic), pp. 511–573.

Chrobak, J.J., and Amaral, D.G. (2007). Entorhinal cortex of the monkey: VII. intrinsic connections. J. Comp. Neurol. *500*, 612–633.

Couey, J.J., Witoelar, A., Zhang, S.J., Zheng, K., Ye, J., Dunn, B., Czajkowski, R., Moser, M.B., Moser, E.I., Roudi, Y., and Witter, M.P. (2013). Recurrent inhibitory circuitry as a mechanism for grid formation. Nat. Neurosci. *16*, 318–324.

Cullen, K.E., and Taube, J.S. (2017). Our sense of direction: progress, controversies and challenges. Nat. Neurosci. *20*, 1465–1473.

Czajkowski, R., Sugar, J., Zhang, S.J., Couey, J.J., Ye, J., and Witter, M.P. (2013). Superficially projecting principal neurons in layer V of medial entorhinal cortex in the rat receive excitatory retrosplenial input. J. Neurosci. *33*, 15779–15792.

de Villers-Sidani, E., Tahvildari, B., and Alonso, A. (2004). Synaptic activation patterns of the perirhinal-entorhinal inter-connections. Neuroscience *129*, 255–265.

Deshmukh, S.S., and Knierim, J.J. (2011). Representation of non-spatial and spatial information in the lateral entorhinal cortex. Front. Behav. Neurosci. *5*, 69.

Desikan, S., Koser, D.E., Neitz, A., and Monyer, H. (2018). Target selectivity of septal cholinergic neurons in the medial and lateral entorhinal cortex. Proc. Natl. Acad. Sci. USA *115*, E2644–E2652.

Doeller, C.F., Barry, C., and Burgess, N. (2010). Evidence for grid cells in a human memory network. Nature *463*, 657–661.

Dolorfo, C.L., and Amaral, D.G. (1998). Entorhinal cortex of the rat: organization of intrinsic connections. J. Comp. Neurol. *398*, 49–82.

Eichenbaum, H. (2017). On the integration of space, time, and memory. Neuron *95*, 1007–1018.

Eichenbaum, H., Yonelinas, A.P., and Ranganath, C. (2007). The medial temporal lobe and recognition memory. Annu. Rev. Neurosci. *30*, 123–152.

Fuchs, E.C., Neitz, A., Pinna, R., Melzer, S., Caputi, A., and Monyer, H. (2016). Local and distant input controlling excitation in layer II of the medial entorhinal cortex. Neuron *89*, 194–208.

Furtak, S.C., Ahmed, O.J., and Burwell, R.D. (2012). Single neuron activity and theta modulation in postrhinal cortex during visual object discrimination. Neuron *76*, 976–988.

Hafting, T., Fyhn, M., Molden, S., Moser, M.B., and Moser, E.I. (2005). Microstructure of a spatial map in the entorhinal cortex. Nature *436*, 801–806.

Honda, Y., and Ishizuka, N. (2004). Organization of connectivity of the rat presubiculum: I. Efferent projections to the medial entorhinal cortex. J. Comp. Neurol. *473*, 463–484.

Høydal, O.A., Skytøen, E.R., Andersson, S.O., Moser, M.B., and Moser, E.I. (2019). Object-vector coding in the medial entorhinal cortex. Nature *568*, 400–404.

Insausti, R., and Amaral, D.G. (2008). Entorhinal cortex of the monkey: IV. Topographical and laminar organization of cortical afferents. J. Comp. Neurol. *509*, 608–641.

Insausti, R., Amaral, D.G., and Cowan, W.M. (1987). The entorhinal cortex of the monkey: II. Cortical afferents. J. Comp. Neurol. *264*, 356–395.

Insausti, R., Herrero, M.T., and Witter, M.P. (1997). Entorhinal cortex of the rat: cytoarchitectonic subdivisions and the origin and distribution of cortical efferents. Hippocampus *7*, 146–183.

Jacobs, J., Weidemann, C.T., Miller, J.F., Solway, A., Burke, J.F., Wei, X.X., Suthana, N., Sperling, M.R., Sharan, A.D., Fried, I., and Kahana, M.J. (2013). Direct recordings of grid-like neuronal activity in human spatial navigation. Nat. Neurosci. *16*, 1188–1190.

Jones, B.F., and Witter, M.P. (2007). Cingulate cortex projections to the parahippocampal region and hippocampal formation in the rat. Hippocampus *17*, 957–976.

Julian, J.B., Keinath, A.T., Marchette, S.A., and Epstein, R.A. (2018). The neurocognitive basis of spatial reorientation. Curr. Biol. *28*, R1059–R1073.

Kerr, K.M., Agster, K.L., Furtak, S.C., and Burwell, R.D. (2007). Functional neuroanatomy of the parahippocampal region: the lateral and medial entorhinal areas. Hippocampus *17*, 697–708.

Killian, N.J., Jutras, M.J., and Buffalo, E.A. (2012). A map of visual space in the primate entorhinal cortex. Nature *491*, 761–764.

Kjonigsen, L.J., Lillehaug, S., Bjaalie, J.G., Witter, M.P., and Leergaard, T.B. (2015). Waxholm Space atlas of the rat brain hippocampal region: three-dimensional delineations based on magnetic resonance and diffusion tensor imaging. Neuroimage *108*, 441–449.

Kobayashi, Y., and Amaral, D.G. (2007). Macaque monkey retrosplenial cortex: III. Cortical efferents. J. Comp. Neurol. *502*, 810–833.

Kobro-Flatmoen, A., and Witter, M.P. (2019). Neuronal chemo-architecture of the entorhinal cortex: A comparative review. Eur. J. Neurosci. Published online July 10, 2019. https://doi.org/10.1111/ejn.14511.

Koganezawa, N., Gisetstad, R., Husby, E., Doan, T.P., and Witter, M.P. (2015). Excitatory postrhinal projections to principal cells in the medial entorhinal cortex. J. Neurosci. *35*, 15860–15874.

Köhler, C. (1984). Morphological details of the projection from the presubiculum to the entorhinal area as shown with the novel PHA-L immunohistochemical tracing method in the rat. Neurosci. Lett. *45*, 285–290.

Köhler, C. (1986). Intrinsic connections of the retrohippocampal region in the rat brain. II. The medial entorhinal area. J. Comp. Neurol. *246*, 149–169.

Kondo, H., and Witter, M.P. (2014). Topographic organization of orbitofrontal projections to the parahippocampal region in rats. J. Comp. Neurol. *522*, 772–793.

Leitner, F.C., Melzer, S., Lütcke, H., Pinna, R., Seeburg, P.H., Helmchen, F., and Monyer, H. (2016). Spatially segregated feedforward and feedback neurons support differential odor processing in the lateral entorhinal cortex. Nat. Neurosci. *19*, 935–944.

Maass, A., Berron, D., Libby, L.A., Ranganath, C., and Düzel, E. (2015). Functional subregions of the human entorhinal cortex. eLife *4*, e06426.

Mathiasen, M.L., Hansen, L., and Witter, M.P. (2015). Insular projections to the parahippocampal region in the rat. J. Comp. Neurol. *523*, 1379–1398.

McNaughton, B.L., Battaglia, F.P., Jensen, O., Moser, E.I., and Moser, M.B. (2006). Path integration and the neural basis of the 'cognitive map'. Nat. Rev. Neurosci. *7*, 663–678.

Miao, C., Cao, Q., Moser, M.B., and Moser, E.I. (2017). Parvalbumin and somatostatin interneurons control different space-coding networks in the medial entorhinal cortex. Cell *171*, 507–521.e17.

Montchal, M.E., Reagh, Z.M., and Yassa, M.A. (2019). Precise temporal memories are supported by the lateral entorhinal cortex in humans. Nat. Neurosci. *22*, 284–288.

Moser, E.I., Moser, M.B., and McNaughton, B.L. (2017). Spatial representation in the hippocampal formation: a history. Nat. Neurosci. *20*, 1448–1464.

Naber, P.A., Caballero-Bleda, M., Jorritsma-Byham, B., and Witter, M.P. (1997). Parallel input to the hippocampal memory system through peri- and postrhinal cortices. Neuroreport *8*, 2617–2621.

Navarro Schröder, T., Haak, K.V., Zaragoza Jimenez, N.I., Beckmann, C.F., and Doeller, C.F. (2015). Functional topography of the human entorhinal cortex. eLife *4*, e06738.

Nilssen, E.S., Jacobsen, B., Fjeld, G., Nair, R.R., Blankvoort, S., Kentros, C., and Witter, M.P. (2018). Inhibitory connectivity dominates the fan cell network in layer II of lateral entorhinal cortex. J. Neurosci. *38*, 9712–9727.

Nilssen, E.S., Doan, T.P., Nigro, M.J., Ohara, S., and Witter, M.P. (2019). Neurons and networks in the entorhinal cortex: A reappraisal of the lateral and medial entorhinal subdivisions mediating parallel cortical pathways. Hippocampus, Published August 13, 2019. https://doi.org/10.1002/hipo.23145.

Ohara, S., Onodera, M., Simonsen, O.W., Yoshino, R., Hioki, H., Iijima, T., Tsutsui, K.I., and Witter, M.P. (2018). Intrinsic projections of layer Vb neurons to layers Va, III, and II in the lateral and medial entorhinal cortex of the rat. Cell Rep. *24*, 107–116.

Papp, E.A., Leergaard, T.B., Calabrese, E., Johnson, G.A., and Bjaalie, J.G. (2014). Waxholm Space atlas of the Sprague Dawley rat brain. Neuroimage *97*, 374–386.

Pastoll, H., Solanka, L., van Rossum, M.C., and Nolan, M.F. (2013). Feedback inhibition enables θ-nested γ oscillations and grid firing fields. Neuron *77*, 141–154.

Paxinos, G., and Watson, C. (2007). The Rat Brain in Stereotaxic Coordinates (Academic).

Peck, J.R., and Taube, J.S. (2017). The postrhinal cortex is not necessary for landmark control in rat head direction cells. Hippocampus *27*, 156–168.

Petreanu, L., Mao, T., Sternson, S.M., and Svoboda, K. (2009). The subcellular organization of neocortical excitatory connections. Nature *457*, 1142–1145.

Ramsden, H.L., Sürmeli, G., McDonagh, S.G., and Nolan, M.F. (2015). Laminar and dorsoventral molecular organization of the medial entorhinal cortex revealed by large-scale anatomical analysis of gene expression. PLoS Comput. Biol. *11*, e1004032.

Ranganath, C., and Ritchey, M. (2012). Two cortical systems for memory-guided behaviour. Nat. Rev. Neurosci. *13*, 713–726.

Reagh, Z.M., and Yassa, M.A. (2014). Object and spatial mnemonic interference differentially engage lateral and medial entorhinal cortex in humans. Proc. Natl. Acad. Sci. USA *111*, E4264–E4273.

Rodo, C., Sargolini, F., and Save, E. (2017). Processing of spatial and non-spatial information in rats with lesions of the medial and lateral entorhinal cortex: Environmental complexity matters. Behav. Brain Res. *320*, 200–209.

Rowland, D.C., Weible, A.P., Wickersham, I.R., Wu, H., Mayford, M., Witter, M.P., and Kentros, C.G. (2013). Transgenically targeted rabies virus demonstrates a major monosynaptic projection from hippocampal area CA2 to medial entorhinal layer II neurons. J. Neurosci. *33*, 14889–14898.

Sargolini, F., Fyhn, M., Hafting, T., McNaughton, B.L., Witter, M.P., Moser, M.B., and Moser, E.I. (2006). Conjunctive representation of position, direction, and velocity in entorhinal cortex. Science *312*, 758–762.

Saunders, R.C., and Rosene, D.L. (1988). A comparison of the efferents of the amygdala and the hippocampal formation in the rhesus monkey: I. Convergence in the entorhinal, prorhinal, and perirhinal cortices. J. Comp. Neurol. *271*, 153–184.

Schultz, H., Sommer, T., and Peters, J. (2012). Direct evidence for domain-sensitive functional subregions in human entorhinal cortex. J. Neurosci. *32*, 4716–4723.

Solstad, T., Boccara, C.N., Kropff, E., Moser, M.B., and Moser, E.I. (2008). Representation of geometric borders in the entorhinal cortex. Science *322*, 1865–1868.

Steffenach, H.A., Witter, M., Moser, M.B., and Moser, E.I. (2005). Spatial memory in the rat requires the dorsolateral band of the entorhinal cortex. Neuron *45*, 301–313.

Stensola, H., Stensola, T., Solstad, T., Frøland, K., Moser, M.B., and Moser, E.I. (2012). The entorhinal grid map is discretized. Nature *492*, 72–78.

Suzuki, W.A., and Amaral, D.G. (1994). Topographic organization of the reciprocal connections between the monkey entorhinal cortex and the perirhinal and parahippocampal cortices. J. Neurosci. *14*, 1856–1877.

Suzuki, W.A., and Porteros, A. (2002). Distribution of calbindin D-28k in the entorhinal, perirhinal, and parahippocampal cortices of the macaque monkey. J. Comp. Neurol. *451*, 392–412.

Tahvildari, B., and Alonso, A. (2005). Morphological and electrophysiological properties of lateral entorhinal cortex layers II and III principal neurons. J. Comp. Neurol. *491*, 123–140.

Tang, Q., Burgalossi, A., Ebbesen, C.L., Sanguinetti-Scheck, J.I., Schmidt, H., Tukker, J.J., Naumann, R., Ray, S., Preston-Ferrer, P., Schmitz, D., and Brecht, M. (2016). Functional architecture of the rat parasubiculum. J. Neurosci. *36*, 2289–2301.

Tsao, A., Moser, M.B., and Moser, E.I. (2013). Traces of experience in the lateral entorhinal cortex. Curr. Biol. *23*, 399–405.

Tsao, A., Sugar, J., Lu, L., Wang, C., Knierim, J.J., Moser, M.B., and Moser, E.I. (2018). Integrating time from experience in the lateral entorhinal cortex. Nature *561*, 57–62.

Uva, L., Grüschke, S., Biella, G., De Curtis, M., and Witter, M.P. (2004). Cytoarchitectonic characterization of the parahippocampal region of the guinea pig. J. Comp. Neurol. *474*, 289–303.

Van Cauter, T., Camon, J., Alvernhe, A., Elduayen, C., Sargolini, F., and Save, E. (2013). Distinct roles of medial and lateral entorhinal cortex in spatial cognition. Cereb. Cortex *23*, 451–459.

van Groen, T., and Wyss, J.M. (1990). The postsubicular cortex in the rat: characterization of the fourth region of the subicular cortex and its connections. Brain Res. *529*, 165–177.

Vaudano, E., Legg, C.R., and Glickstein, M. (1991). Afferent and efferent connections of temporal association cortex in the rat: a horseradish peroxidase study. Eur. J. Neurosci. *3*, 317–330.

Wang, C., Chen, X., Lee, H., Deshmukh, S.S., Yoganarasimha, D., Savelli, F., and Knierim, J.J. (2018). Egocentric coding of external items in the lateral entorhinal cortex. Science *362*, 945–949.

Wilson, D.I., Langston, R.F., Schlesiger, M.I., Wagner, M., Watanabe, S., and Ainge, J.A. (2013a). Lateral entorhinal cortex is critical for novel object-context recognition. Hippocampus *23*, 352–366.

Wilson, D.I., Watanabe, S., Milner, H., and Ainge, J.A. (2013b). Lateral entorhinal cortex is necessary for associative but not nonassociative recognition memory. Hippocampus *23*, 1280–1290.

Winter, S.S., Clark, B.J., and Taube, J.S. (2015). Spatial navigation. Disruption of the head direction cell network impairs the parahippocampal grid cell signal. Science *347*, 870–874.

Witter, M.P., Groenewegen, H.J., Lopes da Silva, F.H., and Lohman, A.H.M. (1989). Functional organization of the extrinsic and intrinsic circuitry of the parahippocampal region. Prog. Neurobiol. *33*, 161–253.

Witter, M.P., Doan, T.P., Jacobsen, B., Nilssen, E.S., and Ohara, S. (2017). Architecture of the entorhinal cortex: a review of entorhinal anatomy in rodents with some comparative notes. Front. Syst. Neurosci. *11*, 46.

Wyss, J.M., and Van Groen, T. (1992). Connections between the retrosplenial cortex and the hippocampal formation in the rat: a review. Hippocampus *2*, 1–11.

Yonelinas, A.P., and Ritchey, M. (2015). The slow forgetting of emotional episodic memories: an emotional binding account. Trends Cogn. Sci. *19*, 259–267.

STAR★METHODS

KEY RESOURCES TABLE

REAGENT or RESOURCE	SOURCE	IDENTIFIER
Antibodies		
Goat anti-PHA-L	Vector Laboratories	#AS-2224
Donkey anti-goat (AF 405, 488, 546, 633)	Invitrogen	#ab175664, #A-11055, #A-11056, #A-21082
Rabbit anti-Cb	Swant	#CB38
Guinea pig anti-NeuN	Sigma Aldrich	#ABN90P
Mouse anti-PV	Sigma Aldrich	#P3088
Mouse anti-PV	Merck Millipore	# MAB1572
Donkey anti-rabbit (AF 488, 546, 633)	Invitrogen	#A-21206, #A10040, #A-21071
Donkey anti guinea pig (AF 488, 546, 633)	Invitrogen	#A-11073, #A-11074, #A-21105
Donkey anti mouse (AF 488, 546, 633)	Invitrogen	#A21202, #A10036, #A-21082
Chicken anti-GFP	Abcam	#ab13970
Mouse anti-Re	Merck Millipore	#MAB5364
Goat anti-mouse (AF 405)	Thermo Fisher Scientific	#A31553
Goat anti-chicken (AF 488)	Thermo Fisher Scientific	#A-11039
Goat anti-rabbit (AF 633)	Thermo Fisher Scientific	# 35562
Bacterial and Virus Strains		
AAV1.hSyn.ChR2(H134R)-eYFP.WPRE.hGH	UPenn Vector Core	#CS0581
Biological Samples		
Normal Goat Serum	Abcam	#AB7481
Chemicals, Peptides, and Recombinant Proteins		
Biotinylated dextran amine	Invitrogen	#D1956
Conjugated dextran amine (AF 488, 546)	Invitrogen	#D22910, #D22911
Phaseolus vulgaris leucoagglutinin	Vector Laboratories	#L-1110
Fast Blue	EMS Chemie	#9000002
Fluorogold	Fluorochrome	#fluoro-gold
Cholera toxin Subunit B 555	Invitrogen	# C22843
Tagged streptavidin (AF 405, 488, 546, 633)	Invitrogen	#S11225, # S21375, # S32354, # S32351
Biocytin	Iris Biotech	#B4261
Tetrodotoxin	Tocris Bioscience	#1078
Bicuculline	Sigma-Aldrich	#14343
Paraformaldehyde	Merck Chemicals	#16005
Dimethyl sulfoxide	VWR	#23486
Deposited Data		
Rat Hippocampus Atlas online dataset	http://cmbn-navigator.uio.no/rat_hippocampus_atlas	N/A
Waxholm SD rat atlas v2	https://www.nitrc.org/projects/whs-sd-atlas	N/A
Experimental Models: Organisms/Strains		
Rat Long Evans	Charles River	#006
Rat Wistar	Charles River	#003
Rat Sprague Dawley	Charles River	#400
Software and Algorithms		
Adobe Photoshop CS6	Adobe Systems	N/A
Adobe Illustrator CS6	Adobe Systems	N/A
Patchmaster	Heka Elektronik	N/A

(*Continued on next page*)

Continued

REAGENT or RESOURCE	SOURCE	IDENTIFIER
MATLAB	MathWorks	N/A
ITK snap	Upenn / UNC	N/A
Amira	Thermo Fisher Scientific	N/A
Material		
Stereotaxic frame	Kopf Instruments	N/A
Stereotaxic frame SR-5R	Narishige	N/A
Glass micropipette	Harvard Apparatus	N/A
PP-830 puller	Narishige	N/A
Digital Midgard Precision current source	Stoelting	N/A
Microinjection pump WPI Nanoliter 2010	Heco	N/A
Freezing microtome	Thermo Scientific	N/A
Menzel-glass slides	Thermo Scientific	N/A
Axio Imager M1/2	Zeiss	N/A
Axio Scan Z1	Zeiss	N/A
Leica VT1000S	Leica Biosystems	N/A
Borosilicate glass capillaries	Harvard Apparatus	N/A
Axio Examiner D1	Zeiss	N/A
EPC 10 Quadro USB amplifier	Heka Elektronik	N/A
UGA-42 GEO point scanning system	Rapp OptoElectronic	N/A
Flex isolation unit	AMPI	N/A
LSM 880 AxioImager Z2	Zeiss	N/A

LEAD CONTACT AND MATERIALS AVAILABILITY

Further information and requests for resources and reagents should be directed to and will be fulfilled by the Lead Contact, Menno P. Witter (menno.witter@ntnu.no). This study did not generate new unique reagents.

EXPERIMENTAL MODEL AND SUBJECT DETAILS

In total, 100 adult female and male Wistar (200-230 g), Sprague Dawley (200-260 g) and Long Evans (190-320 g) rats, including animals from previous projects from our lab (Naber et al., 1997; Koganezawa et al., 2015), were used for the neuroanatomical studies (Tables S1 and S2). Thirteen female and male Long Evans rats aged between P14 and P21 were used for the electrophysiological studies. We did not perform analysis of the influence of sex in the present study at these fundamental neuroanatomical pathways are certainly conserved across genders. Animals were group housed with food and water available *ad libitum*. After surgery, the animals were individually housed until euthanasia. All experiments using male Wistar rats (Table S2) were performed at Tohoku University and conducted according to the Guidelines of the National Institutes of Health and the Tohoku University Guidelines for Animal Care and Use. All remaining experiments were performed at the Kavli Institute for Systems Neuroscience/Centre for Neural Computation at the Norwegian University of Science and Technology (NTNU) where animals were housed and handled according to the Norwegian laws and regulations concerning animal welfare and animal research. Experimental protocols were approved by the Norwegian Animal Research Authority and were in accordance with the European Convention for the Protection of Vertebrate Animals used for Experimental and Other Scientific Purposes.

METHOD DETAILS

Surgeries

Methods for tracer injections have been described in detail previously (Koganezawa et al., 2015). Briefly, under deep isoflurane gas-induced anesthesia, rats were mounted in a stereotaxic frame (Kopf Instruments, Tujunga, CA) and were injected with anterograde or retrograde tracers or adeno-associated virus using coordinates derived from a stereotaxic brain atlas (Paxinos and Watson, 2007) adjusted according to the weight of adult rats or 0.2mm from Bregma, 4.0mm lateral to the sagittal sinus and 2.2mm deep from the brain surface for younger rats (P14-21). Regarding the retrograde tracer injections to LEC from the lateral side (Table S2), the rats were deeply anaesthetized with ketamine (80.0 mg/kg, i.p.) and xylazine (0.8 mg/kg, i.p.) and were mounted in a stereotaxic

frame (Narishige, SR-5R). The lateral skull was exposed, and a burrhole was drilled to visualize the caudal rhinal vein. The injection was conducted ventral to the caudal rhinal vein at a 30-45 degree angle in the coronal plan, with the glass micropipette pointing to the midline.

Anterograde tracers consisted of 10 kDa biotinylated dextran amine (BDA, Invitrogen, Molecular Probes, Eugene, OR; 5% solution in 0.125 M phosphate buffer, pH 7.4), 10kDa preconjugated dextran amines (Alexa 488 or −546 DA; Invitrogen, Molecular Probes, Eugene, OR; 5% solution in 0.125 M phosphate buffer, pH 7.4) and Phaseolus vulgaris leucoagglutinin (PHA-L, Vector Laboratories; 2.5% solution in 10 mM phosphate buffer, pH 7.4). Animals received between 1-4 iontophoretic anterograde tracer injections via a glass micropipette (20–25 μm tip diameter, 30–0044, Harvard Apparatus; pulled with a PP-830 puller) connected to a current source (alternating 6 s on/off current of 7 μA in case of PHA-L and 6 μA in case of BDA and DA for 5-15min, 51595; Stoelting Midgard current source) into various portions of POR and PER (Table S1; Video S1). As retrograde tracers, we used Fast Blue (FB; 1% in PBS, EMS Chemie), Fluorogold (FG; 2.5% in H2O, Fluorochrome) and Cholera toxin Subunit B 555 (CTB555; 4% in H2O, Invitrogen). Animals received between 1-2 retrograde tracer pressure injections via a glass micropipette (30-60 μm tip diameter, 30–0044, Harvard Apparatus, Holliston, MA; pulled with a PP-830 puller) connected to an automated microinjection pump (WPI Nanoliter 2010, Heco) into various portions of MEC and LEC (Table S2; Video S2). For electrophysiological studies, younger rats (age 14 – 21 days postnatally) received pressure injections of adeno-associated virus 1 mediated targeted expression of channelrhodopsin-2-eYFP (AAV1.hSyn.ChR2 H134R-eYFP.WPRE, Addgene) via a glass micropipette (30-40 μm tip diameter, 30–0044, Harvard Apparatus, Holliston, MA; pulled with a PP-830 puller) connected to an automated microinjection pump (WPI Nanoliter 2010, Heco) into various portions of caudal POR. All animals were given a dose of buprenorphine (temgesic, RB Pharmaceuticals, 0.05 mg/kg, subcutaneously) 30 min before the end of the surgery, to reduce postsurgical pain. Upon completion of injections, the wound was cleaned and sutured, and the animal was put back in its home cage.

Histology and immunohistochemistry of neuroanatomical tracing slices

After 7–14 d of survival, adult rats received an overdose of equithesin (a mixture of chloral hydrate, magnesium sulfate, and sodium-pentobarbital; 11 mg/kg body weight i.p.; Sanofi Sante). They were subsequently transcardially perfused with 200 mL of a fresh filtrated oxygenated Ringer's solution (0.85% NaCl, 0.025% KCl, 0.02% NaHCO3, 4°C, brought to pH 6.9 with CO2) followed by 200 mL 4% filtrated freshly depolymerized PFA (1.04005; Merck) in PBS at 4°C. Subsequently, the brain was removed from the skull and postfixed at 4°C in the same fixative for minimum of 2 hours and stored overnight in a mixture of 20% glycerol (VWR, no.24387.292) and 2% dimethyl sulfoxide (DMSO; VWR, no.23486.297). We cut 30-50μm thick brain sections with a freezing microtome (Thermo Scientific) and stored them in 4-6 equally spaced series in the DMSO solution (Table S1). In sections, we visualized BDA with fluorophore-tagged streptavidin (Invitrogen, Molecular Probes, Alexa Fluor 405, 488, 546 or 633), PHA-L with primary (goat anti-PHA-L, Vector Laboratories) and fluorophore-tagged secondary (donkey anti-goat, Invitrogen, Molecular Probes, Alexa Fluor 405, 488, 546 or 633) antibodies. In the case of animals in which both anterograde tracers were injected or had concomitant preconjugated dextran amines injections, we used fluorophores with different emission wave-lengths to discriminate between them and the respective anterograde labeling. For delineation purpose, adjacent series were immunostained for the neuronal stain NeuN and calcium-binding proteins parvalbumin (PV) and calbindin D-28 (Cb) with primary (rabbit anti-Cb, Swant; guinea pig anti-NeuN, Sigma Aldrich; mouse anti-PV, Sigma Aldrich Merck Millipore) and fluorophore-tagged secondary (donkey -anti-rabbit, -guinea pig or -mouse for Cb, NeuN and mouse immunostaining respectively, Invitrogen, Molecular Probes, Alexa Fluor 488, 546 or 633) antibodies. For all immunohistochemical staining, we used the same procedure. Sections were rinsed 3 × 10 minutes in 0.125 M phosphate buffer (PB; pH 7.4) followed by 60 min blocking and permeabilization in 0.125 M PBS-Tx (0.5% Triton X-100, 10% normal goat serum, pH 7.6). Sections were incubated with the primary antibody (1:1000 in PBS-Tx; 48h at 4°C), rinsed 3 × 10 minutes (PBS-Tx) and incubated with the secondary antibody and/or streptavidin (1:200, PBS-Tx, overnight at 4°C, pH 7.6). Finally, sections were rinsed 2 × 10 min in PB 0.125M and then 2 × 10min in a Tris buffer (0.606% Tris(hydroxymethyl)aminomethane, pH 7.6) before being mounted on Menzel-glass slides (Thermo Scientific) from a Tris-gelatin solution (0.2% gelatin in Tris-buffer, pH 7.6) and coverslipped with entelan in a toluene solution (Merck Chemicals, Darmstadt, Germany). When needed, we used the similar protocol on remaining series that were previously delineated using dark-field or cresyl violet from previous studies (Naber et al., 1997; Koganezawa et al., 2015; Table S1).

POR borders and delineations

POR is a six layered cortex located caudal to PER and mostly dorsal to the rhinal fissure where it rises steeply and wraps obliquely around the caudal pole of EC. POR is composed of a ventral (PORv) and a dorsal (PORd) subdivision (Burwell, 2001). POR cytoarchitecture features a homogeneous neuronal distribution across layers II–IV and a resulting lack of a prominent laminar structure. Nonetheless, PORd cells in layer III appear more organized with a clear radial appearance that is absent in PORv (Burwell, 2001). Similar to A35, PORv is completely devoid of parvalbumin (PV) positivity, while PORd stains stronger for PV similarly to A36. The distribution of Cb neuropil in PORv is also similar to that in area 35 and 36 respectively. PORv is bordered ventrally by EC for the most part, which is however replaced caudomedially by a highly variable dorsolateral PaS extension (Burgalossi et al., 2011; Boccara et al., 2015; Ramsden et al., 2015; Tang et al., 2016). PV staining makes these borders stand out since MEC and PaS superficial layers stain strongly for PV, contrary to PORv. In contrast, a marked Cb staining in POR is noticeable, which is absent from PaS or the directly adjacent layers III-VI of EC (Boccara et al., 2015).

PER borders and delineations

PER is a six layered cortex that runs almost parallel with the rhinal fissure, occupying the fundus and/or its dorsal and ventral banks and also comprises a ventral (A35) and a dorsal (A36) subdivision (Burwell et al., 1995). The posterior border of PER is with POR, and is positioned slightly rostral to the ventrally adjacent border between DLE and CE. The rostral border of PER is with the insular cortex and it is generally accepted that this border in coronal sections coincides with the emergence of the claustrum deep to the insular cortex (Burwell, 2001). The border between EC and A35 is indicated by the loss of the typical lamina dissecans in LEC. The superficial layers of A35 are homogeneously packed with small neurons whereas DLE demonstrates a a clear lamination in its superficial layers with layer II cells being larger and more darkly stained than layer III cells. Besides, superficial layers of DLE stain heavily for PV, while staining is essentially absent in A35. Vice versa, in material stained for Cb, a marked increase of staining in area 35 is noticeable.

EC borders and delineations

EC is a six layered cortex delineated by the rhinal fissure on its lateral and dorsal side. In the current paper, we divide EC into MEC composed of caudal (CE) and medial (ME) subdivisions, and LEC composed of dorsal lateral (DLE), dorsal intermediate (DIE) and ventral intermediate (VIE) subdivisions (Insausti et al., 1997). Each EC subdivision is differentiated based on subtle cytoarchitectonic differences and mainly serve detailed anatomical comparisons, but a general pattern is that deep layers (V–VI) are clearly distinguishable from superficial layers (II–III), as the thin acellular layer IV, i.e., lamina dissecans, separates them and this is particularly well developed in MEC. In the present paper, a border of interest is between the two MEC subdivisions, i.e., areas CE and ME. The most striking change that defines this border is an overall less conspicuous lamination in ME than in CE. The superficial layers of ME are less homogeneous than their CE counterparts, ME layer II breaks up into two or three clusters of cells, which makes it less sharply delineated from both layers I and III, and ME layer III tends to split into sublayers. Differences exist also in the superficial portion of their deep layers (layer Va, in opposition to layer Vb) as CE layer Va is sparsely populated by large pyramidal cells, and ME is characterized by a more regularly structured layer Va with a higher number of large pyramidals positioned at regular intervals. Finally, the superficial layers of ventral CE exhibit moderate homogeneous reactivity for parvalbumin, unlike ME where the staining is less strong to absent.

PaS borders and delineations

PaS is a six layered cortex wedged in between PrS and EC, whose most dorsal portion forms a dorsolateral extension which curves around the most caudodorsal part of MEC. This dorsolateral extension of PaS shows a very variable mediolateral extent, and the more laterally extending part can easily be mistaken for MEC (Burgalossi et al., 2011; Boccara et al., 2015; Ramsden et al., 2015; Tang et al., 2016). A striking feature of PaS is its lack of a clear differentiation between superficial layers II and III, seen in dorsal CE, whereas the neuron diameters are substantially larger than the ones seen in POR. In addition, PaS markedly lacks reactivity for calbindin in its superficial layers, which contrasts with the moderate to strong reactivity for that protein of the superficial layers of EC and POR.

Anatomical tracing studies analysis

Sections were inspected with fluorescence illumination at the appropriate excitation wavelengths (Zeiss Axio Imager M1/2), and digital images were obtained using an automated scanner (Zeiss Axio Scan Z1). We thus obtained a library of POR (n = 64) and PER (n = 23) anterograde injections in brains (n = 64) cut in coronal (n = 25), horizontal (n = 18) and sagittal (n = 21) planes (Table S1) as well as retrograde injections into superficial layers of dorsal MEC (ie. area CE; n = 4) and dorsolateral LEC (ie. areas DIE and DLE; n = 9; Table S2). Precise PHR delineations with the help of NeuN, Parvalbumin and Calbindin immunostaining (Boccara et al., 2015) allowed to plot the center of mass for each injections into the 3D Waxholm space atlas reference frame (Papp et al., 2014) which leveraged possibilities for comprehensive multiplanar comparative analysis corroborating anterograde and retrograde tracing datasets in all three main anatomical plans (Kjonigsen et al., 2015; Videos S1 and S2). All injections were made with distinct tracers in the right hemisphere except for 3 animals that had already received bilateral BDA injections as part of a previous study (Table S1). All images selected for illustration purposes were saved as gray-level images of which the contrast and brightness were equalized using Adobe Photoshop and Illustrator (CS6, Adobe Systems).

Construction of two-dimensional unfolded flatmap

We used the methods described in detail previously (Burwell and Amaral, 1998b). In brief, we used coronal sections from the available Rat Hippocampus Atlas online dataset (http://cmbn-navigator.uio.no/rat_hippocampus_atlas), which includes MEC and LEC subdivisions based on NeuN, Cb and PV stainings (Insausti et al., 1997; Boccara et al., 2015). A subset of the sections used to construct the map are visible with distance from Bregma visible above in mm. The fundus of the rhinal sulcus was marked for use as the alignment point. At more caudal levels, where the rhinal sulcus is little more than a shallow indentation, a point was marked at the center of the indentation. A spreadsheet program (Excel, Microsoft) and Adobe Photoshop and Illustrator (CS6, Adobe Systems) were used to create straight-line and colored EC subdivisions unfolded maps (Figure S5A).

Electrophysiological slice preparation

After 2-3 weeks survival time after AAV injection, acute semicoronal slices were prepared from Long Evans rats (P31-P45) following procedures described in detail previously (Nilssen et al., 2018). In short, the animals were anesthetized with isoflurane and killed by decapitation. The brain was quickly dissected out and placed in ice-cold artificial cerebrospinal fluid (ACSF) containing: 110 mM choline chloride, 2.5 mM KCl, 25 mM D-Glucose, 25 mM NaHCO3, 11.5 mM sodium ascorbate, 3 mM sodium pyruvate, 1.25 mM NaH2PO4, 100 mM D-Mannitol, 7 mM MgCl2 and 0.5 mM CaCl2. PH was adjusted to 7.4, and osmolality to 430 mOsm. 400 μm thick slices from the brain hemisphere ipsilateral to the POR injection site were acquired using a vibrating slicer (Leica VT1000S, Leica Biosystems). The slices were cut with an angle of approximately 20° with respect to the coronal plane to preserve the connection between PER and LEC (de Villers-Sidani et al., 2004). Slices were kept at 35° in ACSF containing 126 mM NaCl, 3 mM KCl, 1.2 mM Na2HPO4, 10 mM D-glucose, 26 mM NaHCO3, 3 mM MgCl2 and 0.5 mM CaCl2. The slices were then maintained at room temperature for at least 30 minutes before transferred one-by-one to the recording chamber.

In vitro electrophysiology protocol

Patch clamp recording pipettes (resistance:3-8 MΩ) were made from borosilicate glass capillaries (1.5 outer diameter x 0.86 inner diameter; Harvard Apparatus) and back-filled with internal solution of the following composition: 120 mM K-gluconate, 10 mM KCL, 10 mM Na2-phosphocreatine, 10 mM HEPES, 4 mM Mg-ATP, 0.3 mM Na-GTP, with pH adjusted to 7.3 and osmolality to 300-305 mOsm. Biocytin (5mg/mL; Iris Biotech) was added to the internal solution in order to recover cell morphology. Acute slices were moved to the recording setup and visualized using infrared differential interference contrast optics aided by a 20x/1.0 NA water immersion objective (Zeiss Axio Examiner D1, Carl Zeiss). Electrophysiological recordings were performed at 35°C and slices superfused with oxygenated recording ACSF containing 126 mM NaCl, 3 mM KCl, 1.2mM Na2HPO4, 10 mM D-Glucose, 26 mM NaHCO3 1.5 mM MgCl2 and 1.6 mM CaCl2. Layer IIa of LEC was identified by the presence of large cells aggregated in small clusters. Layer IIb of LEC was identified based on its smaller-sized cells, usually pyramidal-shaped, situated deep to the large cell islands of layer IIa. Up to three neighboring cells situated near virally transduced fibers were selected for simultaneous recordings. Gigaohm resistance seals were acquired for all cells before rupturing the membrane to enter whole-cell mode. Pipette capacitance compensation was performed prior to entering whole-cell configuration, and bridge balance adjustments were carried out at the start of current clamp recordings. Data acquisition was performed by Patchmaster (Heka Elektronik) controlling an EPC 10 Quadro USB amplifier (Heka Elektronik). Acquired data were low-pass filtered (Bessel filter, 4 kHz) and digitized (10 kHz). No correction was made for the liquid junction potential (13 mV as measured experimentally). Negative and positive current pulses (500 ms, −400 to +500 pA, 50 pA incremental steps, 3 s waiting time between stimuli) were injected into the cells to aid classification of recorded cells as principal cells or interneurons. In a subset of experiments, putative monosynaptic laser-evoked synaptic inputs were isolated by sequential application of tetrodotoxin (TTX, 1μM Tocris Bioscience) followed by combined 4-Aminopyridine (4-AP, 100 μM, Sigma-Aldrich) and TTX (Petreanu et al., 2009). Putative inhibitory potentials were confirmed by bath application of the GABAA-receptor antagonist bicuculline (10 μM, Sigma-Aldrich).

Optogenetic stimulation of POR fibers

Optogenetic stimulation was carried out using a patterned laser scanning device (UGA-42 GEO point scanning system, Rapp OptoElectronic) controlling a continuous diode laser (473 nm). The tissue was illuminated with laser pulses of 1 ms in duration and beam diameters between 20-35 μm. Laser stimuli were delivered at a rate of 1 Hz, irradiating the tissue in a 4x5 grid pattern. The grid stimulation protocol was repeated 5-15 times. Laser intensity (1.5-5.0 mW) was adjusted depending on the virus expression level in the slice for each simultaneously recorded cluster as to evoke sub-threshold membrane potential deflections.

Extracellular stimulation of PER

A tungsten bipolar electrode (tip separation: 150-300 μm) was placed in the superficial layers of PER, directly adjacent to the border to LEC, in agreement with a previous report describing that the main projection to dorsolateral LEC originates from layers II and III of PER (Burwell and Amaral, 1998b). A single pulse stimulation (100 μs, 0.3-3 mA) was generated by an Iso-Flex isolation unit (AMPI, Israel) controlled by Patchmaster. The stimulation protocol was repeated 20-50 times. Slices in which extracellular stimulation did not evoke responses in any of the recorded cells indicated unsuccessful preservation of PER to LEC connectivity and were consequently excluded from the dataset. The individual recorded voltage traces (n = 20-50) during electrical activation of PER were used to compute an average trace.

Histology and immunohistochemistry of electrophysiological slices

Immediately following patch clamp recordings, the slices were exposed to 4% paraformaldehyde (PFA, pH 7.4, Merck Chemicals) for 48 hours at 4°C. Slices from electrophysiological experiments were washed in phosphate buffer (PB, 2x15 min, room temperature) followed by membrane permeabilization in Tris buffered saline containing 0.5% Triton X-100 (TBS-Tx. 5x15 min, room temperature). Next, slices were pretreated for 90 minutes in TBS-Tx containing 10% Normal Goat Serum (NGS, Abcam: AB7481) at room temperature. Slices were incubated with primary antibodies rabbit anti-Cb (1:3000, Swant), chicken anti-GFP (1:500, Abcam) and mouse anti-Re (1:1000, Merck Millipore) for 72 hours at 4°C. Slices were incubated simultaneously with the three primary antibodies. After thorough washing in TBS-Tx (5x15 min), slices were incubated in all four secondary antibodies goat anti-mouse (1:400, AF405,

Thermo Fisher Scientific), goat anti-chicken (1:500, AF488, Thermo Fisher Scientific), fluorescent conjugated streptavidin (1:600, AF546, Thermo Fisher Scientific) and Goat anti-rabbit (1:400, AF633, Thermo Fisher Scientific) for 24 hours at 4°C. Slices were rinsed repeatedly in TBS-Tx (3x15 min) at room temperature and dehydrated by increasing ethanol concentrations (30%, 50%, 70%, 90%, 100%, 100%, 10 min each). They were treated to a 1:1 mixture of 100% ethanol and methyl salicylate for 10 minutes before clearing and storage in methyl salicylate.

Confocal microscopy and EC cell classification

Visualization of recorded cells using laser scanning confocal microscopy and subsequent classification of LEC layer II morphological cell types was described in detail previously (Nilssen et al., 2018). In brief, slices were mounted in methyl salicylate in custom made metal slides and imaged using a laser scanning confocal microscope (Zeiss LSM 880 AxioImager Z2). Single images and z stacks were acquired with low magnification (Plan-Apochromat 10x, NA 0.45 and Plan-Apochromat 20x, NA 0.8). These images were used to determine the morphology of the recorded cells, as well as confirm their position relative to the virally transfected fibers and within LEC molecularly defined (reelin versus calbindin) cell populations. All images were acquired with 8 bit depth. Classification of principal cell morphology was based on their somatodendritic morphology, in line with previously published criteria (Tahvildari and Alonso, 2005; Canto and Witter, 2012; Nilssen et al., 2018). Interneurons had small cell bodies, extensive local axonal ramifications and aspiny dendrites. Principal cells had large somata and dendrites covered with spines. These cells had a main axon that could be traced extending from the cell body toward the deep white matter. Fan cells had a round soma and multiple apical dendrites that ramified superficial to the cell body, creating a fan-like appearance. Few, if any, basal dendrites extending toward deeper layers were present. Pyramidal cells had an elongated, pyramid-shaped, cell body oriented perpendicular to the pia. Pyramidal cells had multiple dendrites extending from the base of the soma, and typically one long apical dendrite extending to the pial surface. Oblique pyramidal cells resembled pyramidal cells but were tilted approximately 45° with respect to the pia. These cells frequently had more than one main apical dendrite. Multiform cells were classified as all cells that did not fall into the other categories. Multiform cells usually had a multipolar morphology without polarization of the dendritic tree, exhibiting both well-developed basal and apical dendrites.

QUANTIFICATION AND STATISTICAL ANALYSIS

Characterization and quantification of POR cells projecting to dorsolateral LEC. Retrograde tracers Cholera toxin Subunit B (CTB; n = 3) or Fluorogold (FG; n = 2) were injected in the dorsolateral LEC of adult rats with regular burrholes (Figure S2B; Video S2; Table S2) in addition to retrograde FG injections (n = 4) deposited directly into superficial layers of dorsolateral LEC through laterally drilled burrholes (Figure S2C; Video S2; Table S2). Quantification of POR retrogradely labeled cells were made in a single serie for each animal using a laser scanning confocal microscope (Zeiss LSM 880 AxioImager Z2). Single images and z stacks were acquired with low magnification (Plan-Apochromat 10x, NA 0.45 and Plan-Apochromat 20x, NA 0.8) with 8 bit depth (Figure S2D). Images were transferred to a Neurolucida system (Neurolucida 360, MicroBrightField) in order to count the total number of retrogradely labeled cells that colocalized with NeuN and Cb at different Z-levels (Figure S2D). At last, we calculated the standard deviation (σ) of POR cells co-expressing Cb and NeuN in each animal groups (Figure S2E).

Quantification of POR axon terminals in MEC and LEC

Normalization of POR axonal terminal densities in MEC and LEC was obtained using the 3 available anterograde flatmaps (Figure S5B) from Burwell and Amaral (1998b). First, we reversed the five-level set of standards designated from none (0) to very light (1), light (2), moderate (3), heavy (4) and very heavy (5) into corresponding numerical values in each MEC and LEC bins. For single bins containing a neighboring region, their numerical value was divided by 2. The percentage of POR axonal terminal was then calculated by dividing the sum of each bin's numerical values by the total amount of bin by area. At last, we calculated the standard deviation (σ) of POR axonal terminals for each animal (Figure S5C).

Optogenetic stimulation of POR fibers

Acquired traces from each stimulation spot (5-15 sweeps) were averaged, producing an average response for each stimulation spot in the grid. Deflections in this overall average trace exceeding 10 standard deviations (±10 SD) of the baseline, defined as the average potential derived from the 50 ms interval prior to laser stimulation onset, were classified as true laser-evoked synaptic responses. The response amplitude of this voltage deflection was measured as the peak voltage minus the baseline potential. Potentials were identified as excitatory if they crossed the threshold to elicit action potential firing, or when depolarizing responses were observed at membrane potentials positive to the calculated chloride reversal potential (−69.2 mV, calculated using the Nernst equation). Inhibitory potentials were hyperpolarizing potentials and/or sensitive to application of bicuculline. Data analyses were conducted using customized scripts in MATLAB (MathWorks).

Extracellular stimulation of PER

Membrane potential deflections were considered stimulus-evoked according to the same criterion as for the optogenetic experiments. The individual voltage traces were used to measure the latency of the postsynaptic potentials, in order to compute the jitter

in the synaptic response. The synaptic jitter was defined as the standard deviation of the latency. Connections in which the synaptic jitter was < 700 μs were classified as presumed monosynaptic (Canto and Witter, 2012). In cases where synaptic latency could not be extracted from the individual traces, the connections were deemed unclassifiable with respect to being mono- or polysynaptic.

DATA AND CODE AVAILABILITY

Data and code to reproduce the analyses reported in the paper will be made available at request via the Witter Lab repository (https://www.ntnu.edu/kavli/research/witter).